

Louis Gagnon provides this scientific self-archived article free of charge.
For more research info see LouisGagnon.com

This article is the final submission, post-review, version of the following article:

Gagnon, L., Richard, M.J., and Lévesque, B., « Simulation of a rotating device that reduces the aerodynamic drag of an automobile », *Trans. Can. Soc. Mech. Eng.*, 35(2):229-249, 2011, url: <http://www.tcsme.org/Papers/Vol35/Vol35No2Paper6.pdf>

Note: The version of this document may differ in format from the official version distributed by the publisher. The scientific content should nevertheless be identical as this version was created after conclusion of the peer-review process. For the official version, please consult the publishers website. Do keep in mind that a subscription or fee may be asked for the official version.

SIMULATION OF A ROTATING DEVICE THAT REDUCES THE AERODYNAMIC DRAG OF AN AUTOMOBILE.

Louis Gagnon, Marc J. Richard, Benoît Lévesque
Département de génie mécanique, Université Laval, Québec (Qc) Canada
Email: louis.gagnon.10@ulaval.ca; marc.richard@gmc.ulaval.ca

Received Month 0000, Accepted Month 0000
No. 00-CSME-00, E.I.C. Accession Number 0000

ABSTRACT

A two-dimensional Computational Fluid Dynamics (CFD) analysis of the Ahmed body is performed using the k-omega-SST turbulence model implemented in the OpenFOAM (OF) software. The analysis is then modified to include a rotating paddle wheel which captures energy from the swirl that forms behind the vehicle. The rotating wheel is implemented using a General Grid Interface (GGI) in the mesh. Flow energy is captured by the wheel and the power generated by the wheel reaches 16.1 W at optimal conditions. Overall drag reductions of up to 7.6% are also found as side-effects of the rotating paddle wheel. Computations are run in parallel on a dual core computer. A mesh of 30,000 cells is used. Y^+ values on the walls of the vehicle range from 60 to 500. Tests are run at both fixed and variable paddle wheel angular velocities.

Keywords: Ahmed body; CFD; active drag reduction; paddle wheel.

RÉSUMÉ

Une analyse de la dynamique des fluides numérique bidimensionnelle du corps Ahmed est effectuée en utilisant le modèle de turbulence k-omega-SST implémenté dans le logiciel OpenFOAM (OF). L'analyse est ensuite modifiée pour inclure une roue à aubes en rotation qui capte l'énergie du tourbillon qui se forme derrière le véhicule. La roue rotative est implémentée en insérant une interface « General Grid Interface » (GGI) dans le maillage. L'énergie de l'écoulement est captée par la roue et la puissance générée par celle-ci atteint 16.1 W aux conditions optimales. Une réduction totale de la traînée de 7.6% est aussi obtenue en tant qu'effet secondaire de la roue à aubes en rotation. Les analyses sont effectuées en parallèle sur un ordinateur à deux processeurs. Un maillage de 30 000 cellules est utilisé. Les valeurs de Y^+ sur les parois du véhicule varient entre 60 et 500. Des tests sont faits à des vitesses constantes et à des vitesses variables de la roue à aubes.

Mots-cles: Corps Ahmed; CFD; réduction active de la traînée; roue à aubes.

NOMENCLATURE

A	frontal area of the Ahmed body (m^2)
$C_{D,body}$	drag coefficient of the car-paddle assembly due to the body only
$C_{D,part}$	drag coefficient of the car-paddle assembly due to the paddle only
$C_{D,power}$	power saved by the avoided drag when vehicle travels at 60 m/s (W)
$C_{D,saved}$	reduction of the drag coefficient of the car-paddle assembly incurred by the device
$e_{capture}$	power captured by the wheel (W)
e_{drag}	power required to overcome a drag coefficient at a given traveling velocity (W)
M_z	flow-incurred moment about the lateral axis of the wheel (Nm)
R	angular velocity of the paddle wheel (RPM)
R_{var}	angular velocity of the variable-angular-velocity paddle wheel (RPM)
r	radius of the paddle wheel (cm)
T	thickness of the two-dimensional Ahmed body simulation (m)
t	time (s)
U	air velocity far from the Ahmed body of the simulation (m/s)
V	traveling velocity of the Ahmed body (m/s)
w	width of the three-dimensional Ahmed body (m)
x_{center}	distance between the rear vertical wall and the center of the paddle wheel (cm)
Greek symbols	
ρ	density of air (kg/m^3)
ν	kinematic viscosity of air (m^2/s)

1. INTRODUCTION

The aerodynamics of turbulent flows remains a subject of both great interest and great challenge to engineers. Many questions are yet to be answered, and consequently, many opportunities for development can be explored. Flow behavior is an important aspect of most design projects and the reason often is to build safe structures that will withstand the strongest winds. Other times it is important to evaluate the flow behavior to ensure that flow-cooled parts of a system will be cooled properly. However, an aspect that has also fascinated many engineers since the dawn of engine-powered travel is the external aerodynamics of vehicles: the resistance of wind to the forward movement of a car, a bus, a train, etc.. A large portion of the energy consumed by ground vehicles is used to overcome pressure drag. Nonetheless, as pointed out by Choi et al. [1], the scientific community still questions whether the optimal drag reduction on a body would equate to a null pressure drag. Countless papers have been published on the subject of reducing the drag coefficient of a vehicle [2–8]. In an attempt to bring new ideas to the table, this paper shows how moving parts can be added to an automobile to reduce the energy it consumes to overcome wind resistance. That is achieved by capturing energy from the swirls of the flow located behind a hatchback car. The energy is captured by a rotating device located within the separation bubble of the flow behind the vehicle. That rotating device is inspired by paddle wheels and its purpose is to recapture energy from the vortices located behind a moving vehicle. Although the simulations were performed on a car model, tractor-trailer rigs and any vehicle involved in a lot of high speed driving are ideal candidates for the type of device presented in this paper.

2. THE CAR MODEL

The Ahmed car model is chosen as the shape to analyze in the simulations because it has received widespread attention from the scientific community since its first appearance when Ahmed et al. [9] used it in a wind tunnel to mimic the flow found around a typical car. The model is also used by the European Research Community On Flow, Turbulence, And Combustion (ERCOFTAC) to benchmark different CFD methods. The geometry of the Ahmed body is shown in Fig. 1. The first step of this study is thus to create a CFD case that will reproduce the generally accepted flow characteristics and the drag coefficient of the Ahmed body with minimal error. Numerically reproducing the experimental drag coefficient of the Ahmed body has been a challenge for many researchers that studied the Ahmed body because of the difficulty to precisely locate the start and end of the separation bubble on the rear slant wall of the body. However, a general idea of the appropriate drag coefficient is grasped from the research of Guilmineau [10] to be in the range of 0.25 to 0.35 when the rear slant angle is 25° . It must also be pointed out that between the two widely used angles of 25° and 35° there is a drag crisis. The crisis occurs at roughly 30° and is characterized by the experimental drag coefficient reaching 37.8, as measured by Ahmed et al. [9]. Several attempts were done by different authors to reproduce the transition phenomenon that occurs between those two angles where the flow actually goes from having its longitudinal (streamwise) vortices form on the sides of the rear slant wall of the vehicle to having them start only on the lower, vertical, rear end. Those three-dimensional vortices significantly influence the drag forces on the Ahmed body because they interact with the separation bubble located on the slant wall. However, Beaudoin and Aider [3] have experimentally demonstrated that those vortices can be avoided by use of side wings on the slant wall of the model and that removing them can also reduce drag. Lehugeur et al. [11] also reduced drag when lowering the vorticity of the streamwise vortices to 25% of their original value. They reduced the vorticity by blowing at the location where Beaudoin and Aider [3] had installed side wings. The goal of this project is to deal with the middle, two-dimensional, separation bubble which exists behind the body and hosts two spanwise vortices that meet approximately in the middle of the rear vertical wall of the car. They are shown in Fig. 14 and the kinetic energy of these vortices is what is recaptured by the paddle wheels used in this paper.

3. CFD ANALYSIS

3.1. Governing Equations

The OF solver turbDyMFoam, which is used for all the calculations presented, uses the Unsteady Reynolds-Averaged Navier Stokes (URANS) equations. One can notice that the density ρ does not appear in the incompressible fluid equations and thus the graphical results of pressure given in this paper are actually pressure divided by density. The URANS equations are solved within a PISO loop. Turbulence is incorporated into the URANS equations using the following formulation,

$$\frac{\partial \mathbf{U}}{\partial t} + \nabla \cdot \phi \mathbf{U} = -\nabla p + \nabla \cdot \mathbf{v}_{eff} \nabla \mathbf{U} + \nabla \cdot (\mathbf{v}_{eff} ((\nabla \mathbf{U})^T - \frac{1}{3}(\nabla \cdot \mathbf{U}) \mathbf{I})) \quad (1)$$

where the effective turbulent viscosity is,

$$\mathbf{v}_{eff} = \mathbf{v}_t + \mathbf{v} \quad (2)$$

The turbulence model is described below.

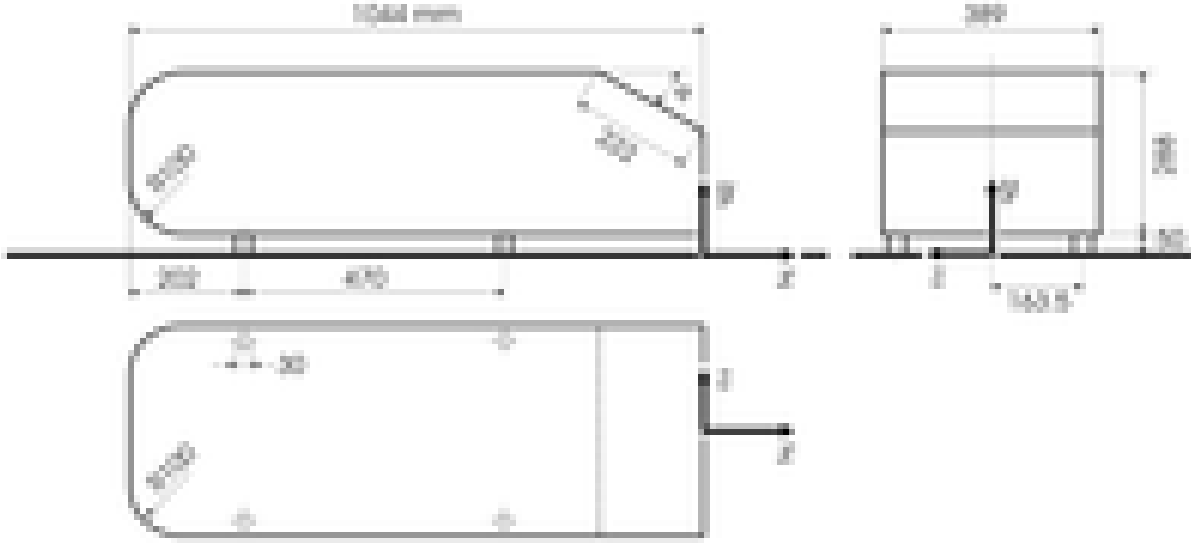


Figure 1: The Ahmed body, adapted from Hinterberger et al. [12] with kind permission of Springer Science+Business Media. Throughout this paper, the x , y , and z axes represent streamwise, vertical, and spanwise directions, respectively.

3.2. Turbulence model

Large Eddy Simulations (LES) turbulence models were considered but not deemed appropriate for two-dimensional modeling even if some authors, such as Bouris and Bergeles [13], have reported successful use of LES in two dimensions. Examples of URANS equations yielding accurate drag coefficients of the Ahmed body are available in the literature [10, 14, 15]. For instance, Guilmineau [10] reports an accurately reproduced flow topology of the Ahmed body but a difficulty of the URANS equations to properly reproduce the experimental separation bubble on the 25° slant wall. The experimental flow exhibits a detached zone at the onset of the slant wall and reattachment at its middle whereas URANS results all show separation along the whole slant wall. The $k-\omega$ -SST model features an automatic wall treatment and uses $k-\omega$ equations within the boundary layer and $k-\epsilon$ equations in the freestream flow; a blending function ensures a smooth transition between the near wall and freestream equations. Considering that Bayraktar et al. [16] found good results using the RNG $k-\epsilon$ model on the Ahmed body, use of $k-\epsilon$ equations in the freestream flow should give reliable results. Near the wall, classical log law wall functions are used because the y^+ values are well above 20.

According to the $k-\omega$ -SST turbulence model, the turbulent viscosity is,

$$\nu_t = \frac{a_1 k}{\max(a_1 \omega, F2 \sqrt{S2})} \quad (3)$$

where a_1 , $F2$, and $S2$ are specified in the OF source code [17]. The turbulent kinetic energy, k , and turbulent frequency, ω , are solved by,

$$\frac{\partial k}{\partial t} + \nabla \cdot (\mathbf{U}k) = \min(G, c_1 \beta^* k \omega) - \beta^* \omega k + \nabla \cdot (\alpha_k \nu_t + \nu) \nabla k \quad (4)$$

and,

$$\frac{\partial \boldsymbol{\omega}}{\partial t} + \nabla \cdot (\mathbf{U}\boldsymbol{\omega}) = 2\gamma S2 - \beta \boldsymbol{\omega}^2 + \nabla \cdot (\alpha_{\omega} \mathbf{v}_t + \mathbf{v}) \nabla \boldsymbol{\omega} - (F1 - 1) \frac{2\alpha_{\omega 2} (\nabla k \cdot \nabla \boldsymbol{\omega})}{\boldsymbol{\omega}} \quad (5)$$

where the values of the undefined constants are found in the source code [17]. A thorough description of the k- $\boldsymbol{\omega}$ -SST turbulence model is given in the paper by Menter and Esch [18].

3.3. Drag forces calculation

In OF, the drag coefficient is calculated by dividing the total force acting on the part of interest, in the drag direction, by the reference area and the dynamic pressure. It is given by the following equation,

$$C_D = \frac{\text{dragForce}}{\text{Aref} \times p\text{Dyn}} \quad (6)$$

where the dynamic pressure is,

$$p\text{Dyn} = 0.5 \times \text{rhoRef} \times \text{magUinf} \times \text{magUinf} \quad (7)$$

In Eqs. (6) and (7), *Aref* is the frontal area of the part and *rhoRef* and *magUinf* are the density and freestream velocity of the fluid, respectively. The total force, *dragForce*, is the sum of both friction and pressure forces in the drag direction, as shown below,

$$\text{dragForce} = \{ \text{rho}(p) \times \sum(\text{pf}) + \sum(\text{vf}) \} \cdot \{ \text{dragDir} \} \quad (8)$$

where *rho(p)* represents the fluid density and *dragDir* is the direction vector in which the drag is calculated. Here, the OF pressure is multiplied by density because, as stated earlier, OF uses *Pascals* divided by density in kg/m^3 as its pressure. $\sum(\text{pf})$ and $\sum(\text{vf})$ are the pressure and friction vectors, respectively. They are summed on the surface of a body and are defined as,

$$\sum(\text{pf}) = \sum_{i=\text{patchi}} (\text{Sfb}_i \times \text{pb}_i) \quad (9)$$

and,

$$\sum(\text{vf}) = \sum_{i=\text{patchi}} (\text{Sfb}_i) \cdot (\text{devRhoRef fb}_i) \quad (10)$$

where *patchi* is an index that represents the cell face on which the drag forces are calculated and covers all the cell faces of the body of interest. *Sfb_i* is a vector having a direction normal to the face of cell *i*. It also has a magnitude equal to the area of the face of cell *i*. *pb_i* and *devRhoRef fb_i* are values of the pressure field, *p*, and of the stress tensor, *devRhoRef*, at the face of cell *i*. When using a k- $\boldsymbol{\omega}$ -SST turbulence model, OF defines the stress tensor as,

$$\text{devRhoRef} = \text{rhoRef} \times -\mathbf{v}_{eff} \times \text{dev}((\nabla U) + (\nabla U)^T) \quad (11)$$

where \mathbf{v}_{eff} is defined by Eq. (2) and *dev* is the deviatoric operator. OF defines it as,

$$\text{dev}(T) = T - \frac{1}{3}(T_{11} + T_{22} + T_{33})I \quad (12)$$

where *T* is a 3×3 matrix and *I* is the identity matrix.

3.4. Parameters and boundary conditions

The air velocity used in the analysis is $U = 60 \text{ m/s}$ and the kinematic viscosity is $\nu = 14.75 \times 10^{-6} \text{ m}^2/\text{s}$. The Reynolds number of this analysis, based on model length, is $Re = 4.25 \times 10^6$. k and ω inlet boundary conditions are calculated from a 0.5% turbulence intensity, as measured by Ahmed et al. [9], and an approximated turbulent length scale of 5 cm. As stated earlier, the rear slant angle of the vehicle is 25° and, on its walls, $60 \leq y^+ \leq 500$.

3.5. Mesh

A Reynolds number of 4.25×10^6 requires a very fine mesh. Due to the changing behavior of the flow close to the Ahmed body, a structured boundary layer mesh is only used at locations of very small tangential gradient of the near-wall flow properties. Thus, only two small zones of the mesh are structured and use about 500 less cells than an equivalent unstructured mesh. Using a boundary layer mesh on the front of the body is not appropriate because the pressure gradient is as strong along the tangent of the surface as along the normal. Using a structured mesh on the rear slant and vertical surfaces is also inappropriate due to sudden changes in pressure at specific locations and a velocity distribution typical of detached flows. It is also necessary to have a well resolved mesh behind the car to properly simulate the wake. The mesh on the wall of the vehicle requires a fine resolution because of its influence on the drag coefficient. The zone just upstream of the vehicle is meshed slightly coarser than the wake because there are no vortices in front of the car. At this location, the flow outside the boundary layer is only influenced by a saddle point. Considering that it is generally recommended to have at least 15 nodes in the boundary layer and that the flat plate boundary layer thickness is estimated, from the formulae given by Cousteix [19], to reach 2 cm, it is not possible to precisely resolve the said layer and the simulations rely on wall models. The mesh of the paddle wheel cases is shown in Fig. 2. It is refined at the tips of the paddles to properly represent their features and smaller cells are also found around the wheel for reasons to be explained in Section 3.6.



Figure 2: Mesh of the vehicle with a paddle wheel.

In their three-dimensional numerical analysis of the Ahmed body, Bayraktar et al. [16] found from mesh refinement tests that a 4.4 million cell unstructured mesh yields a fine correlation between experimental and numerical drag coefficients. It was thus desired to get a two-dimensional mesh

that had roughly the same domain resolution as the analysis of Bayraktar et al. [16]. From their number of cells and the assumption that the relative numbers of cells in the longitudinal, lateral, and vertical directions are a , $0.25a$, and $0.2a$, respectively, it was found using the following equation that an equivalent 2D mesh would have 40 thousand cells,

$$a \times 0.2a \times 0.25a = 4.4 \times 10^6 \implies a = 444.80 \quad \therefore N_{cells,2D} = a \times 0.2a \approx 40,000 \quad (13)$$

where a is the unknown and $N_{cells,2D}$ is the number of cells of the equivalent two-dimensional mesh. The meshes used for the present analysis are slightly rougher and have 27.5 thousand to 34 thousand cells. All meshes are generated by the Gmsh software. Details of the mesh generation software are found in the article by Geuzaine and Remacle [20].

3.6. Rotating interface

A rotating interface, the GGI of the OF software, is used to allow the paddle wheel to rotate with respect to the car. This is accomplished by having the solver interpolate the cell face values of the flow properties at a virtual interface which is indicated to the solver by the definition of two coincident circles that delimit the inner (rotating part) and outer (fixed car) parts of the mesh. Details of the interface solution procedure are given by Gagnon [21] and by the source code [17]. As seen in Fig. 2, the mesh resolution at the interface, to the right of the car, is increased in order to make the interface as close as possible to a perfect circle. This reduces to a minimum the empty zones that occur between the inner and outer parts of the mesh when the two interface polygons rotate with respect to each other. These zones can cause divergence of the solution when they become large.

3.7. Validation

The drag coefficient of the unaltered two-dimensional Ahmed body simulation is used to calculate the drag coefficient differences between the energy-capturing and the reference (unaltered) models. It is thus necessary to have a certain level of confidence towards the solution of the flow around the reference body. This level of confidence is gained by running a mesh refinement test with a mesh that contains twice as many nodes in x and in y directions. The refined mesh has 111.5 thousand cells. A 6% difference between the drag coefficient of the reference mesh and of the refined mesh is found and it is deemed to be a fairly accurate correlation. The simulation with the finer mesh yields a slightly higher drag coefficient and that makes the calculation of total drag reduction by use of the paddle wheel more conservative. As can be seen in Figs. 3 and 4, the flow fields of the refined mesh give a more detailed view of the flow properties but both analyses share the same general flow characteristics. A time-step of 1×10^{-5} second is used for the simulations that use the reference mesh.

The simulations with the added paddle wheel have a roughly equal time step. The Courant number serves as a check to maintain time steps below a value where divergence could occur. It is defined in the following equation,

$$Co = \frac{\delta t |U_c|}{\delta x} \quad (14)$$

where δt is the time step, δx is the length of the cell in the direction of the flow, and $|U_c|$ is the magnitude of the flow velocity through the cell in question. Thus, in presence of the paddle wheel the time steps are continuously adjusted so that $Co \leq 0.5$. This ensures that the calculation remains stable by preventing the fluid from traveling more than half a cell between each time step, as pointed

out in the OF user guide [22]. The Courant number is computed for each cell at each time step and the next time step is adjusted according to the maximum Courant number computed.

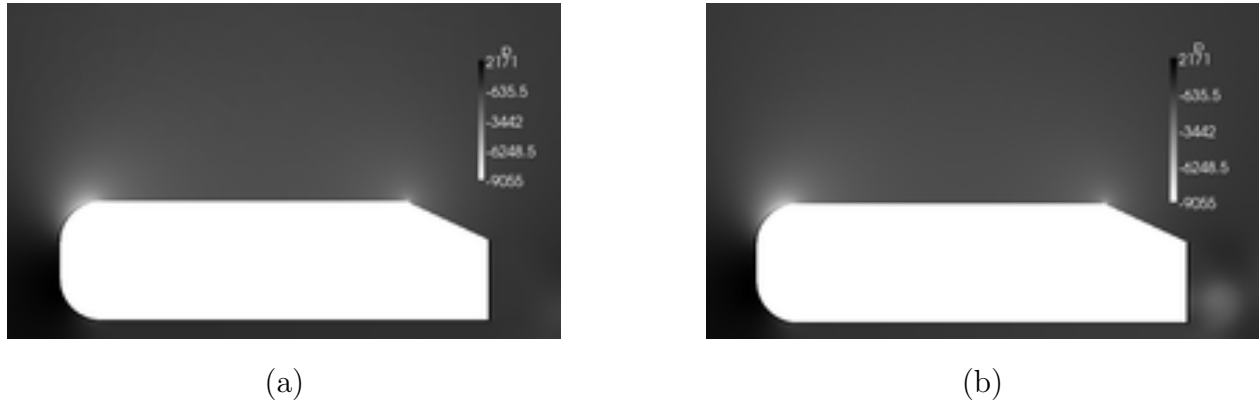


Figure 3: Instantaneous pressure fields of the Ahmed body: a) reference mesh, b) refined mesh.

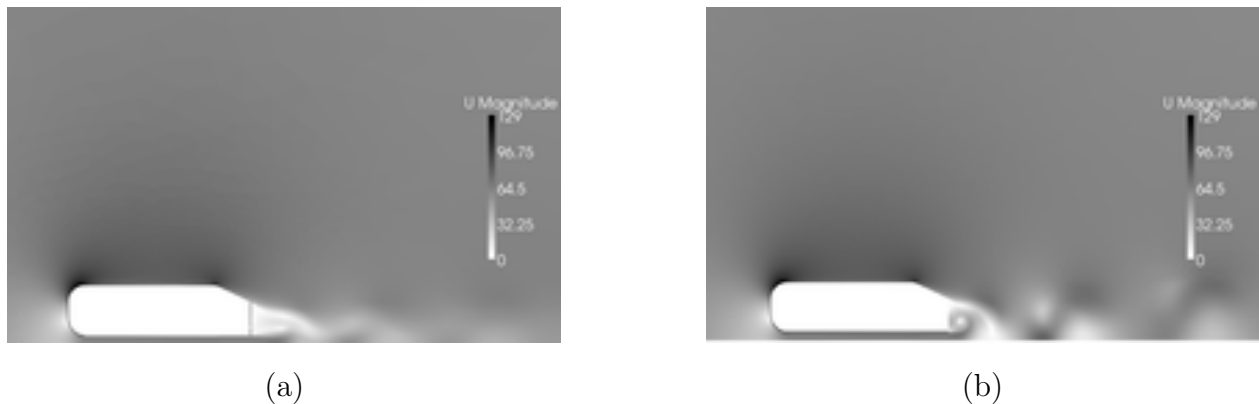


Figure 4: Instantaneous velocity fields of the Ahmed body: a) reference mesh, b) refined mesh.

4. ENERGY CAPTURE

As mentioned in the introduction, the goal is to have an added part that captures energy from the flow. For results to be interesting the total drag with the added part cannot be higher than that of the unaltered Ahmed body. Alternatively, if the total drag is increased then the energy captured from the flow has to surpass the energy lost to drag. To capture the energy, a device inspired by old fashion paddle wheels is inserted behind the vehicle. It is immersed near the center of the upper spanwise vortex. Its location is shown in Fig. 5. Every wheel presented in this paper has 4 paddles. A clockwise angular velocity is imposed to the wheel and the instantaneous amount of power generated is calculated from the moment acting on the paddle. The average power generated over a cycle is obtained when the

stability of the power generation cycle has been reached. Some tests are run with a constant angular velocity and others with a sinusoidal angular velocity. The justification for such a system is that, in a practical application, an electric motor controller would adjust velocity fluctuations by giving power to or taking power from the wheel.

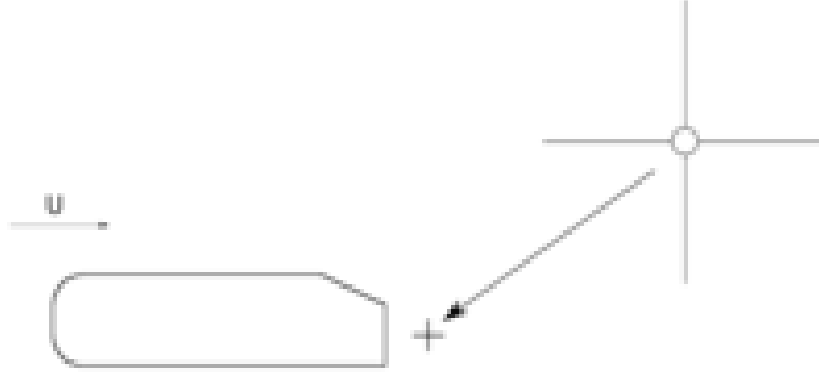


Figure 5: The two-dimensional representation of the Ahmed body with the paddle wheel located behind its rear vertical wall.

To compare energy captured and drag coefficients, the following equation measures how much power is required to overcome a specific drag coefficient at the traveling velocity V of the Ahmed car,

$$e_{drag} = \left(\frac{1}{2} \times \rho \times U^2 \times A \times C_D\right) \times V \quad (15)$$

where C_D is the drag coefficient considered for conversion into equivalent energy. The frontal area A of the three-dimensional Ahmed body is 0.11203 m^2 . The density ρ of the ambient air is 1.2 kg/m^3 . On the other hand, the following equation gives how much power is extracted from the flow by the paddle wheel,

$$e_{capture} = M_z \times \frac{R \times 2\pi}{60} \times \frac{w}{T} \quad (16)$$

where M_z is the moment about the z-axis. R is the rotational velocity of the paddle wheel in revolutions per minute (RPM). The width w of the three-dimensional Ahmed body is 0.389 m and the thickness T of the two-dimensional model used in the analysis is 0.01 m .

5. RESULTS

5.1. Reference body

The reference case gives an average body drag coefficient of 0.2977. This is 3.8% higher than the experimental results of Ahmed et al. [9] who reported 0.2868. The drag value of 0.2977 is used to calculate the coefficient of avoided drag, $C_{D,saved}$, defined by the following equation,

$$C_{D,saved} = 0.2977 - C_{D,body} - C_{D,part} \quad (17)$$

where $C_{D,body}$ and $C_{D,part}$ represent the drag coefficients on the Ahmed body and on the added part, respectively. Then, the power saved by the avoided drag when vehicle travels at 60 m/s, $C_{D,power}$,

is calculated by Eq. (15) using $C_{D,saved}$ as input. It is also found from Eq. (15) that the reference three-dimensional Ahmed car requires 4.36 kW when moving at 60 m/s. The drag force cycle on the reference Ahmed body is 11.85 ms long and exhibits a steady behavior when averaged over a cycle. The time dependent flow behavior of the reference body is shown by the streamlines in Fig. 14.

5.2. Selected cases

5.2.1. Fixed rotational velocity

Results from cases of rotating paddle wheels are compiled in Table 1. The wheel's center of rotation y-position is 19 cm below the top wall of the body. x_{center} is the distance between the rear vertical wall and the center of the paddle wheel and R is its angular velocity. r is the radius of the paddle wheel.

Table 1: Results from selected cases with fixed rotational velocity.

Case	1	2	3	4	5	6
x_{center} (cm)	13.3	16.6	13.3	16.6	13.3	13.3
r (cm)	5	4	5	4	4	5
R (RPM)	2500	2000	2000	4000	2000	2300
$C_{D,body}$	0.3084	0.2939	0.3122	0.2954	0.3130	0.3122
$C_{D,part}$	-0.0323	-0.0148	-0.0335	-0.0207	-0.0353	-0.0334
$C_{D,saved}$	0.0216	0.0186	0.0190	0.0229	0.0204	0.0190
$C_{D,power}$ (W)	313	271	276	333	291	276
$e_{capture}$ (W)	0.9	8.2	12.8	-4.6	6.0	10.4

Figures 6 and 7 illustrate the energy captured and the avoided drag coefficient, respectively, for a full revolution of the paddle wheel of case 3. The wheel is at 0° and 30° at $t = 1.4700s$ and $t = 1.4725s$, respectively. The data is taken from $t = 1.45s$ to $t = 1.48s$, which is long after steadiness of the time-averaged flow has been reached. To illustrate how the flow stabilizes in the first tenths of a second of the simulation, the average power extracted from the wheel of case 6 is plotted against time in Fig. 8 where each calculation is done for one full revolution of the paddle wheel. One full revolution is equivalent to 4 geometric cycles. After time $t = 0.26s$ the average power extracted stabilizes at $e_{capture} = 10.38 \pm 0.01 W$.

The evolution of the flow around the paddle wheel for one geometric cycle is shown for case 3 in Figs. 15, 16, and 17. In Fig. 16 there is one arrow per cell and that explains the appearance of a circle at the GGI interface and the large quantity of arrows at the tips of the paddles. The evolution of the vortices for one geometric cycle can be grasped by looking at the streamlines in Fig. 15. Also for case 3, Fig. 10 shows the power generated by each side, front and back, of a paddle wheel blade for one full revolution. The total power generated by the blade is also shown on the same figure. One can notice that most power is generated by the front part of the paddle. The power cycle is depicted for one paddle but is identical for each of the four paddles with the exception that their cycles are each out of phase by 90° due to their geometrical arrangement.

5.2.2. Variable rotational velocity

The OF GGI code was modified to allow the wheel to rotate according to a sinusoidal function. Results from two such cases are compiled in Table 2. They are both identical to case 3 with the

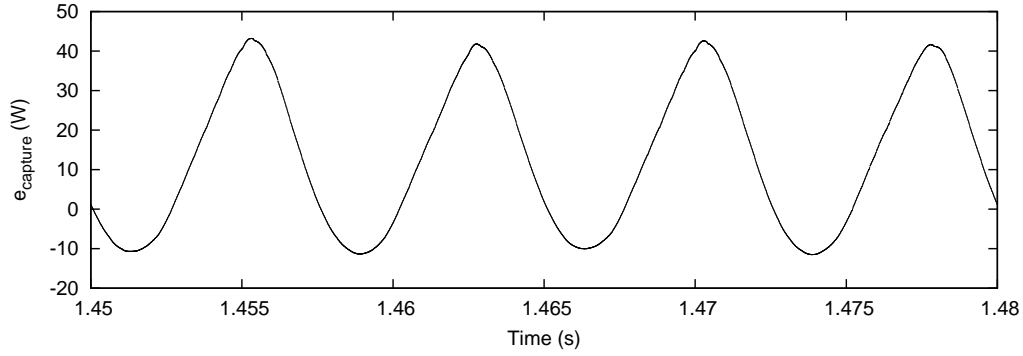


Figure 6: Plot of $e_{capture}$ vs Time for one full revolution of the paddle wheel from case 3.

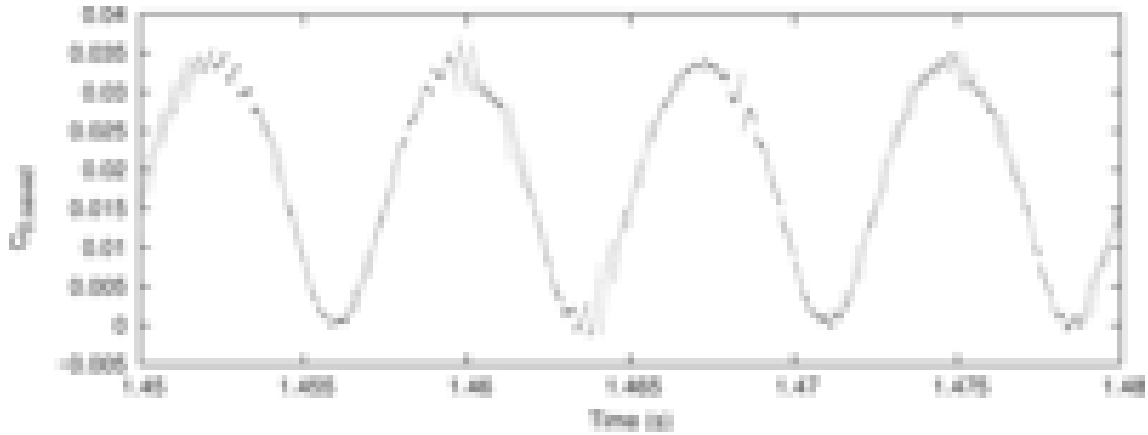


Figure 7: Plot of $C_{D,saved}$ vs Time for one full revolution of the paddle wheel from case 3.

exception that they have a variable angular velocity. Their angular velocities, R_{var} , are defined by the following equations,

$$R_{var,7} = R \times \left[1.0 + 0.2 \times \sin\left(-2.9249 + \frac{R \times \pi}{7.5} \times t\right) \right] \quad (18)$$

$$R_{var,8} = R \times \left[1.0 + 0.2 \times \sin\left(-2.3 + \frac{R \times \pi}{7.5} \times t\right) \right] \quad (19)$$

where R is the average angular velocity, which is 2000 RPM for both cases, and t is time in seconds. Since the power generation cycle has a period exactly equal to a fourth of the period of rotation of the paddle wheel, the frequency of the sinusoidal function is also chosen as such. The only difference between the two cases is the phase angle of the sinusoidal function. $R_{var,7}$ was designed so that the paddle wheel moves at maximum rotational velocity when the maximum power, or maximum M_z , is seen from the results of the constant angular velocity case 3. Thus, the phase angle of the sinusoidal function comes from a graphical approximation of the phase angle of the power output of the wheel from case 3. This phase matching is done in an attempt to reduce fluctuations in the power generated. The attempt is not significantly successful but more power is generated. Power generation and angular velocity are plotted together for one full revolution of the paddle wheel of case 7 in Fig. 9. The sinusoidal angular velocity does not increase the time required to reach a steady average power generation. The

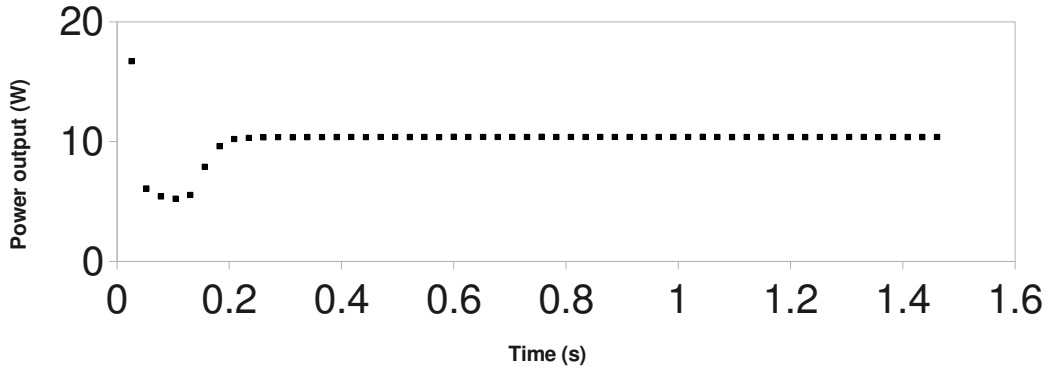


Figure 8: Plot of power output vs time calculated per paddle wheel revolution starting at $t = 0$. Each cycle is 0.0261 seconds long based on the rotational velocity of 2300 RPM. Data taken from case 6.

results of these two cases are given in Table 2.

Table 2: Results from selected cases with variable angular velocity.

Case	7	8
$C_{D,body}$	0.3104	0.3095
$C_{D,part}$	-0.0335	-0.0342
$C_{D,saved}$	0.0208	0.0225
$C_{D,power}$ (W)	302	327
$e_{capture}$ (W)	16.1	12.0

5.3. Comparison cases

It is questioned whether the reduced drag is only due to the modification of the shape of the Ahmed model by the presence of the paddle wheels. Therefore, some cases of non-rotating and modified paddle wheels are tested. Results of these cases are summarized in Table 3. The added parts have their center 13.3 cm behind the rear wall and 19 cm below the top wall and have a radius of 5 cm. Cases 0° and 30° model a fixed paddle wheel rotated by 0° and 30° from the horizontal position, respectively. Case A models a paddle wheel whose inner radius was enlarged to 0.045 m which makes it almost a cylinder. Case B is a copy of case A with the exception that the object revolves at 2500 RPM. Power consumed by the paddle wheel of case B is 1.28 W. Case C is a 5 cm radius cylinder that does not rotate. Case D is an attempt at making the rear of the Ahmed body more streamlined in order to compare the drag avoided by this streamlined rear with the drag reduced by various wheel configurations. Graphical representations of the comparison cases are given in Table 3 and a detailed view of each case is given in Figs. 11 to 13.

6. DISCUSSION

Several configurations of the paddle wheel are tested. The most average power captured from the flow is 16.1 W and the maximum instantaneous power generation reaches three times that. These

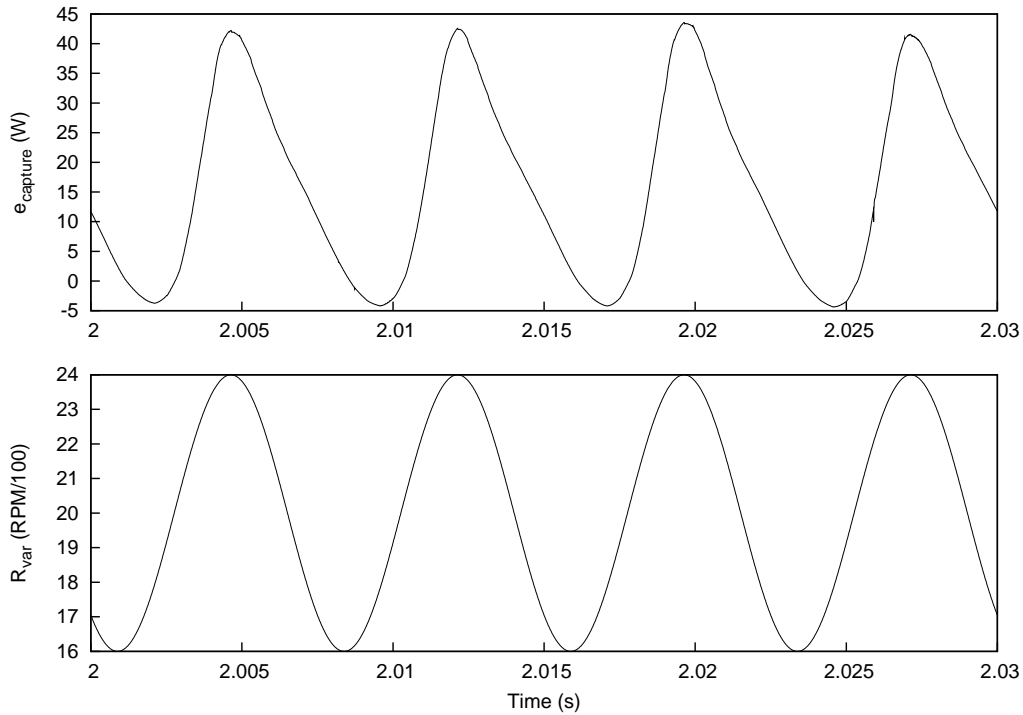


Figure 9: Plot of $e_{capture}$ and R vs Time for one full revolution of the variable angular velocity paddle wheel from case 7.

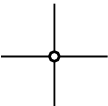
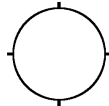
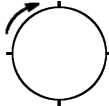
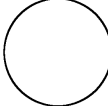
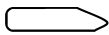
results are seen in case 7 which models a 5 cm radius paddle wheel rotating at an average R of 2000 RPM. The rotating paddle wheel configuration of case 4 reduces the drag coefficient the most and is a paddle wheel rotating at 4000 RPM, located slightly upwind of the maximum turbulent kinetic energy location, and having a radius of 4 cm. This drag reduction is closely followed by the variable angular velocity wheel of case 7.

The results show that paddle wheels that let the flow cross their center do not yield as much energy and are therefore not documented in this paper. A filled center is deemed necessary because it serves to prevent incoming flow from being diverted between the paddles and wasting its kinetic energy. It is also noticed that the paddles should not interfere with the flow traveling outside of the separation bubble since results show that doing so increases drag without increasing the amount of power generated.

Non-rotating paddle wheels do not reduce the drag coefficient. The fixed 0° and 30° paddle wheels add to the total drag of the Ahmed body whereas when the rotating wheel of case 3 is at 0° and 30° , the instantaneous avoided drags, $C_{D,saved}$, are 0.0083 and 0.0152, respectively. In fact, the instantaneous avoided drag never goes above 0.0008 and 0.0065 for the 0° and 30° fixed paddle wheel cases, respectively. This supports the idea that the effect of the rotation of the paddle wheel is paramount to the drag reduction. Comparison cases C and D reduce the total drag coefficient of the assembly and it is an expected result because those cases present more streamlined bodies. However, since the intent here is not to modify the shape of the car but rather to have an added part which generates energy and possibly reduces drag, those two cases were not further investigated.

From Figs. 14 and 15 it is seen that the spanwise vortices are influenced by presence of the rotating paddle wheel and this partly explains why the overall drag coefficient is reduced. For instance, the

Table 3: Results from comparison cases where a negative $C_{D,power}$ indicates that the power demand is increased.

Case	0°	30°	A	B	C	D
$C_{D,body}$	0.3111	0.3063	0.3099	0.3288	0.3107	0.2151
$C_{D,part}$	-0.0046	-0.0069	-0.0392	-0.0351	-0.0551	-
$C_{D,saved}$	-0.0088	-0.0017	0.0269	0.0038	0.0422	0.0826
$C_{D,power}$ (W)	-128	-25	391	55	612	1199
						

upper spanwise vortex creates a suction on the upstream side of the paddle wheel and thus decreases the total drag force. This effect is not beneficial to the overall drag coefficient when the paddle wheel does not revolve. There is less turbulent kinetic energy in the cases with the paddle wheel and this indicates that less energy is lost by viscous dissipation.

From the analysis, it seems clear that the angular velocity is highly influential on the energy output of the system. The best results are obtained at an average R of 2000 RPM. As expected, when the angular velocity of the paddle wheel reaches a certain value, the power generated turns into power that has to be fed to the wheel. On the other hand, for very small angular velocities, the forces on the paddle wheel do not increase enough to compensate for its lower velocity and thus the power generated decreases. When taking into account that a full revolution of the paddle wheel corresponds to four quarter cycles that are each geometrically identical, the fluctuations in energy captured and drag coefficient have the same period as the geometrical rotation of the paddle wheel; this is seen on Figs. 6 and 7. Four force cycles occur for each complete revolution of the paddle wheel. In contrast, the reference Ahmed body showed a force cycle that would be expected from a paddle wheel rotating at 1266 RPM. The fact that the best result comes from a variable rotational speed wheel shows the potential for the energy capture to be adapted to the flow. In order to have the angular velocity of the paddle wheel adapt to the flow, an algorithm where the angular velocity of the paddle wheel is a function of the forces that act on it is currently being developed. It will be able to extract a specific amount of power from the flow and this will help simulate a paddle wheel that recaptures energy in the form of electricity by use of an electronically-controlled motor tuned to capture a specific amount of power. The energy spent to overcome the inertia of the paddle wheel in the variable angular velocity cases is not considered into the calculation of the power captured since it cancels itself out after each velocity cycle and since power-generation and geometrical cycles have the same period. In a more advanced analysis, where a paddle wheel would be built, the inertia should be taken into account in the calculation of the angular velocity. Gas-electric hybrid vehicles would suit as good candidates for such a system because they already have high capacity batteries on-board.

As seen in Figs. 16 and 17, the flow modified by the rotating paddle wheel creates a low pressure zone at the tip of the paddle every time it passes through the topmost point of the cycle. That low pressure zone leaves the blade at a velocity greater than that of the paddle itself and is one of the two main forces driving the wheel. The other driving force is the large difference of pressure between

the front and the back of the paddle when it goes through its bottommost point. The fact that most power is generated by the front part of the paddle indicates that a more streamline shape for the rear of the paddle would likely increase the amount of power generated.

The total energy reduction is calculated from the extrapolation of the two-dimensional simulations to a three-dimensional body. This extrapolation should hold as long as a device similar to what is reported by Beaudoin and Aider [3] or by Lehugeur et al. [11] is used to eliminate the influence of the streamwise vortices on the spanwise vortices.

In the published literature, most of all Ahmed body analyses are run with a fixed floor, and that is different from real-world situations where the floor has a relative velocity with respect to the car equal to the velocity of the car itself. This does not drastically modify the results but it was reported by Krajnovic and Davidson [23] to have a 8% influence on the drag coefficient and a noticeable influence on the flow near the rear wall of the car. That zone is where this paper is focused but the purpose here is to show how flow structures found on a typical car can be used to generate energy. Specific car models are not analyzed yet and the Ahmed body is only used to recreate typical car flows and validate the calculations.

The results obtained with the $k-\omega$ -SST model in two dimensions are fairly reasonable and the flow on the rear slant wall stays attached for the whole wall. A small low pressure zone appears at the onset of the slant wall. These results compare well with the 25° experimental slant wall center-line flow which detaches and reattaches quickly, as reported by Guilmineau [10]. Moreover, Guilmineau noted that three-dimensional analyses with URANS model were not able to predict the reattachment on the rear slant wall and thus the use of such a model cannot be tuned to perfection.

Finally, it should be noted that more tests have to be run in order to yield results of greater energy capture and drag reduction. The authors believe that it is possible to get a positive energy capture to accompany results of large drag reduction given by the non-moving cylinder but that the good combination of angular velocity and blade geometry has yet to be found.

7. CONCLUSION

It is found that the rotating paddle wheel can generate a sustained 16.1 W while reducing drag by 6.9%. The instantaneous power generation nearly reaches 50 W. The device can also reduce drag by 7.6% if power is supplied to the paddle wheel. There is less turbulent kinetic energy in the flow and the vortices behind the car are weakened when the wheel is present. The position and angular velocity of the paddle wheel have an important impact on the results. A variable angular velocity paddle wheel seems to be a more efficient energy capturing device than a constant angular velocity wheel. Using modified blade shapes and different variable angular velocities is expected to greatly improve the efficiency of the device. Once a two-dimensional optimum is obtained and confirmed by refined meshes the next step is to conduct three-dimensional and experimental tests. Who knows, with increasingly electric vehicles, maybe this type of flow-interacting device can evolve into something more than just an energy capturing device?

8. ACKNOWLEDGMENTS

The authors are grateful to the Natural Sciences and Engineering Research Council of Canada for supporting this research. We would also like to thank everyone who contributed to the development of the open-source software that was used to conduct this research.

REFERENCES

1. Choi, H., Jeon, W.P. and Kim, J., "Control of flow over a bluff body," *Annual Review of Fluid Mechanics*, Vol. 40, pp. 113–139, 2008.
2. Bruneau, C.H., Gilliéron, P. and Mortazavi, I., "Flow manipulation around the Ahmed body with a rear window using passive strategies," *Comptes Rendus Mécanique*, Vol. 335, No. 4, pp. 213–218, 2007.
3. Beaudoin, J.F. and Aider, J.L., "Drag and lift reduction of a 3D bluff body using flaps," *Experiments in Fluids*, Vol. 44, No. 4, pp. 491–501, 2008.
4. Bruneau, C.H., Creusé, E., Depeyras, D., Gilliéron, P. and Mortazavi, I., "Coupling active and passive techniques to control the flow past the square back Ahmed body," *Computers & Fluids*, Vol. 39, pp. 1875–1892, 2010.
5. Cowperthwaite, N., "An investigation of the effect of rear body pitch on the aerodynamic characteristics of a simplified tractor-trailer model," *Journal of Wind Engineering and Industrial Aerodynamics*, Vol. 22, pp. 215–226, 1986.
6. Gilhaus, A., "The influence of cab shape on air drag of trucks," *Journal of Wind Engineering and Industrial Aerodynamics*, Vol. 9, pp. 77–87, 1981.
7. Watkins, S. and Vio, G., "The effect of vehicle spacing on the aerodynamics of a representative car shape," *Journal of Wind Engineering and Industrial Aerodynamics*, Vol. 96, pp. 1232–1239, 2008.
8. Barnard, R. and Vaughan, H., "The aerodynamic tuning of a group C sports racing car," *Journal of Wind Engineering and Industrial Aerodynamics*, Vol. 22, pp. 279–289, 1986.
9. Ahmed, S.R., Ramm, G. and Faltin, G., "Some salient features of the time averaged ground vehicle wake," Tech. Rep. TP-840300, Society of Automotive Engineers, Warrendale, Pa., 1984.
10. Guilmineau, E., "Computational study of flow around a simplified car body," *Journal of Wind Engineering and Industrial Aerodynamics*, Vol. 96, No. 6-7, pp. 1207–1217, 2008.
11. Lehugeur, B., Gilliéron, P. and Ivanić, T., "Contribution de l'éclatement tourbillonnaire à la réduction de la traînée des véhicules automobiles : approche numérique," *Comptes Rendus Mécanique*, Vol. 334, pp. 368–372, 2006.
12. Hinterberger, C., García-Villalba, M. and Rodi, W., "Large eddy simulation of flow around the Ahmed body," In R. McCallen, F. Browand and J. Ross, eds., "Lecture Notes in Applied and Computational Mechanics, The Aerodynamics of Heavy Vehicles: Trucks, Buses, and Trains," pp. 77–87, Springer Verlag, 2004.
13. Bouris, D. and Bergeles, G., "2D LES of vortex shedding from a square cylinder," *Journal of Wind Engineering and Industrial Aerodynamics*, Vol. 80, pp. 31–46, 1999.
14. Kapadia, S. and Roy, S., "Detached eddy simulation over a reference Ahmed car model," *Proceedings of 41st Aerospace Sciences Meeting and Exhibit*, Reno, Nevada, USA, Jan. 6–9, 2003.
15. Martinat, G., Bourguet, R., Hoarau, Y., Dehaeze, F., Jorez, B. and Braza, M., "Numerical simulation of the flow in the wake of ahmed body using detached eddy simulation and urans modeling," *Advances in Hybrid RANS-LES Modelling*, pp. 125–131, 2008.
16. Bayraktar, I., Landman, D. and Baysal, O., "Experimental and computational investigation of Ahmed body for ground vehicle aerodynamics," *Society of Automotive Engineers Transactions: Journal of Commercial Vehicles*, Vol. 110, No. 2, pp. 613–626, 2001.
17. OpenCFD, *OpenFOAM-dev-1233 source code*, OpenCFD Limited, Berkshire, UK, 2009.
18. Menter, F.R. and Esch, T., "Elements of industrial heat transfer predictions," *Proceedings of the 16th Brazilian congress of mechanical engineering (COBEM)*, Uberlandia, Brazil, Nov. 26–30, 2001.
19. Cousteix, J., *Turbulence et couche limite*, Cépaduès Éditions, 1989.
20. Geuzaine, C. and Remacle, J.F., "Gmsh: a three-dimensional finite element mesh generator with built-in pre- and post-processing facilities," *International Journal for Numerical Methods in Engineering*, Vol. 79,

No. 11, pp. 1309–1331, 2009.

21. Gagnon, L., *Calcul de la résistance aérodynamique d'un véhicule muni de pièces en mouvement*, Master's thesis, Université Laval, Québec, 2010.
22. OpenCFD, *OpenFOAM user guide*, OpenCFD Limited, Berkshire, UK, 2008.
23. Krajnovic, S. and Davidson, L., "Influence of floor motions in wind tunnels on the aerodynamics of road vehicles," *Journal of Wind Engineering and Industrial Aerodynamics*, Vol. 93, pp. 677–696, 2005.

APPENDIX: LARGE FIGURES

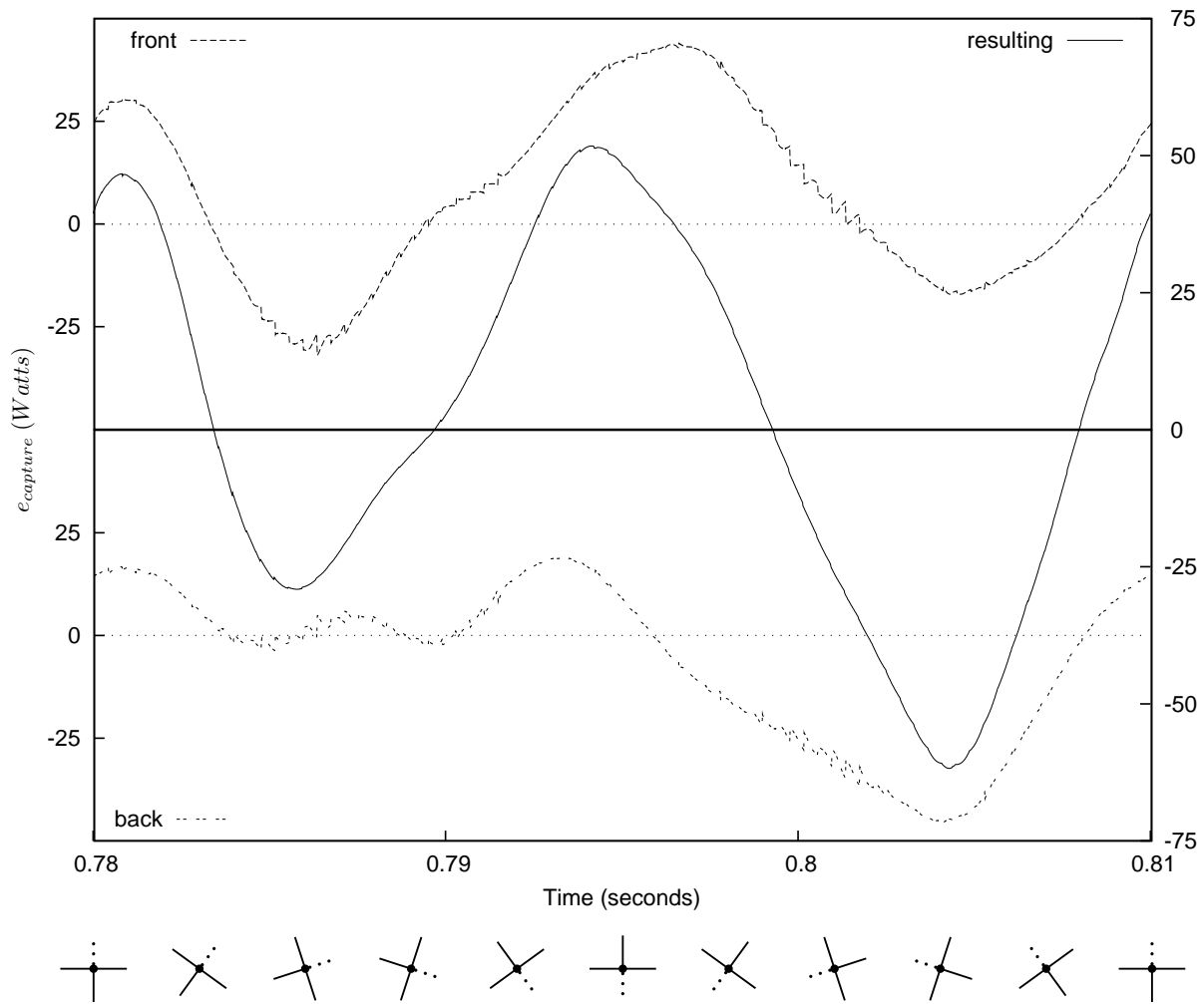


Figure 10: Plot of $e_{capture}$ vs Time for one paddle, depicted below the graph. The left y-axis serves for the front and the back of the paddle and the right y-axis serves for the total power generated by that paddle. Data taken from case 3.

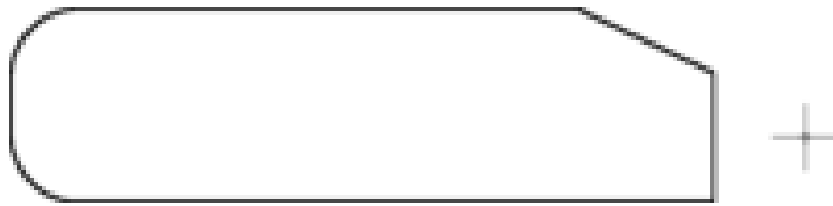


Figure 11: Ahmed body with added part. Case 0° .

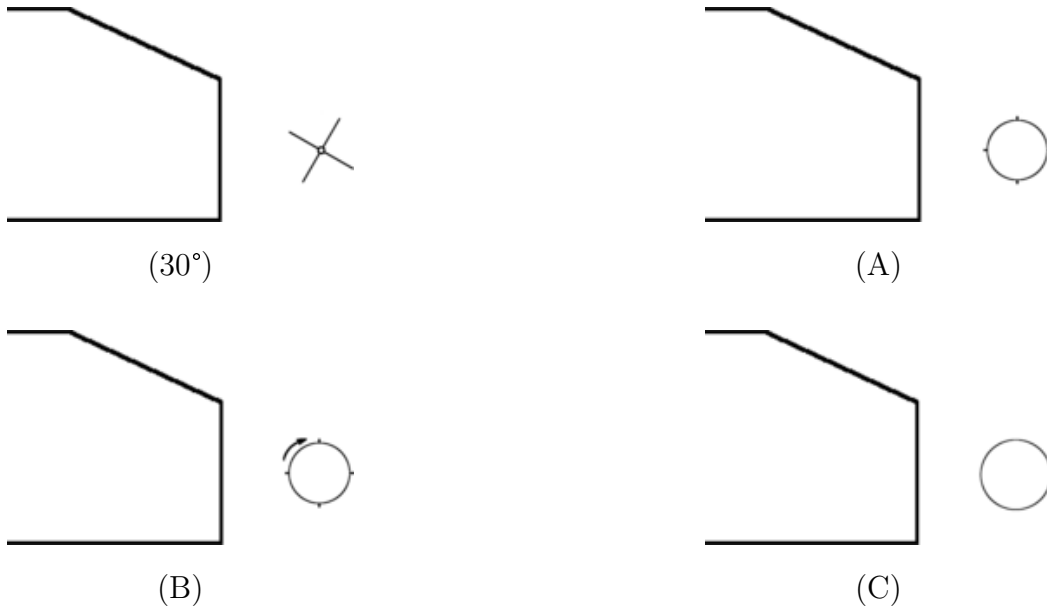


Figure 12: Rear of the Ahmed body with added part: cases 30° , A, B, and C.



Figure 13: Modified Ahmed body. Case D.

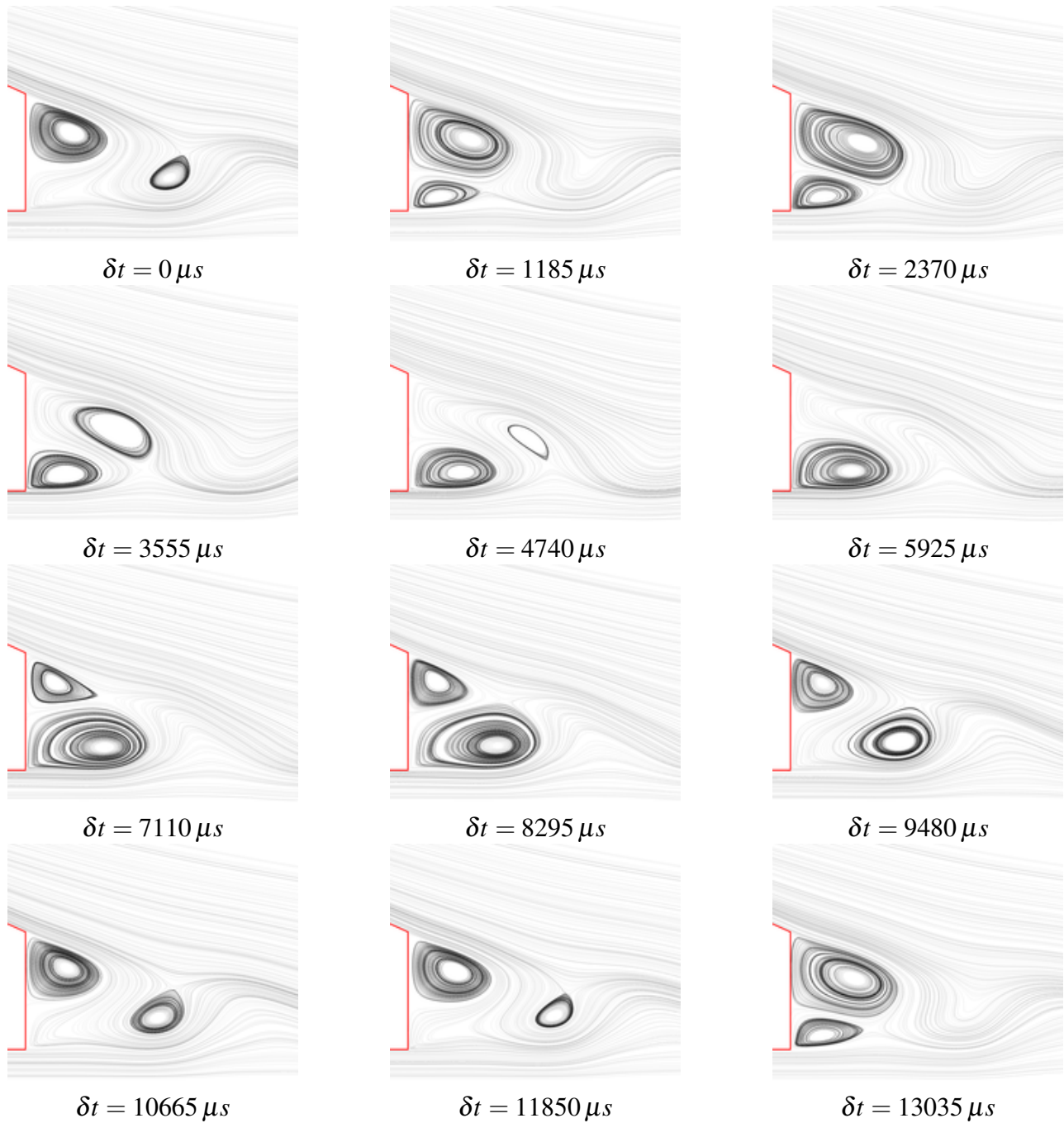


Figure 14: Streamlines of the flow behind the reference Ahmed body for one drag force cycle ($11850 \mu s$). The cyclic flow behavior is apparent when comparing the last two snapshots with the first ones. The color and density of the streamlines have no meaning here.

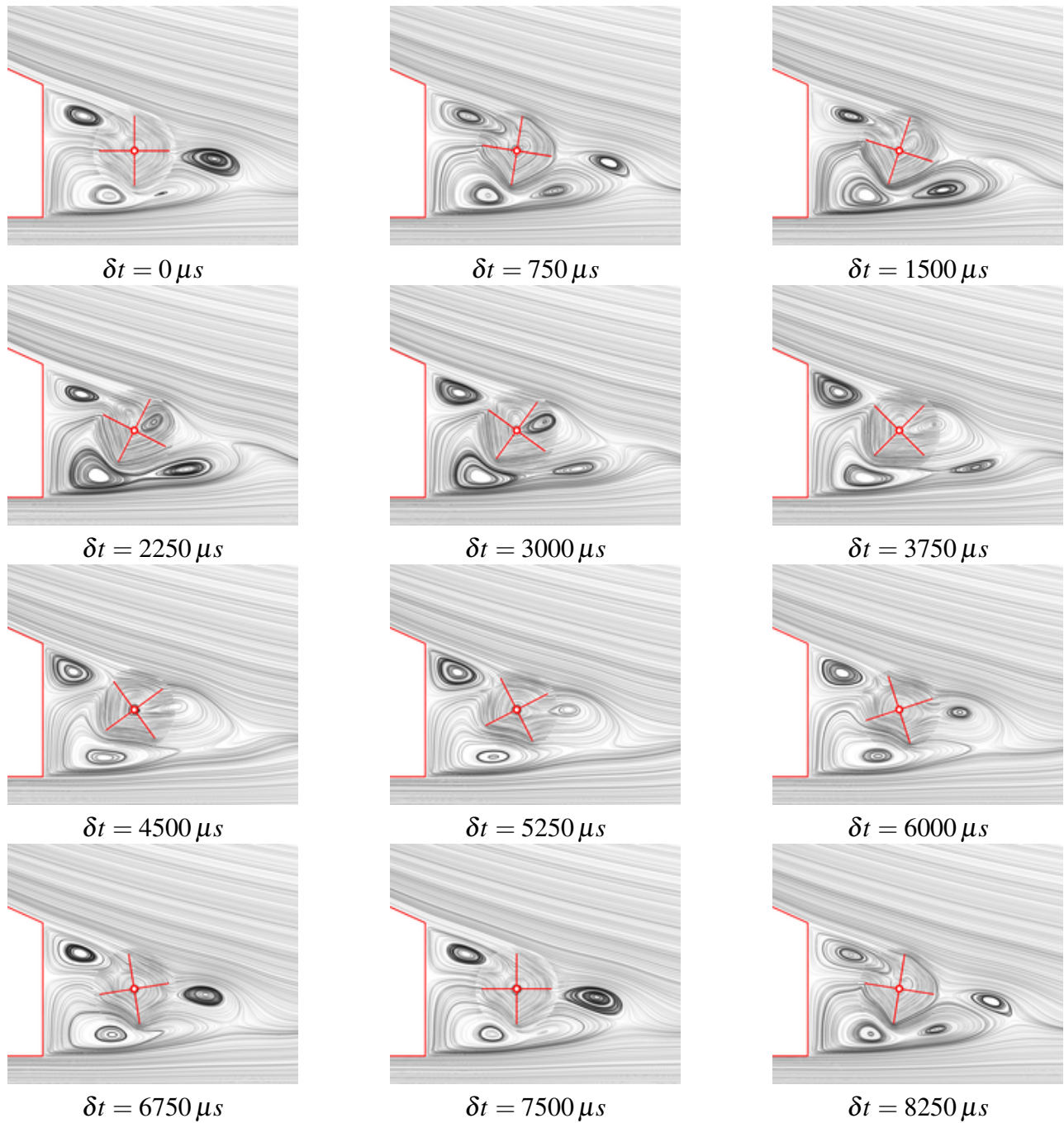


Figure 15: Streamlines of the flow behind the Ahmed body of paddle wheel case 3 for one geometrical cycle ($7500 \mu s$). The cyclic flow behavior is apparent when comparing the last two snapshots with the first ones. The color and density of the streamlines have no meaning here.

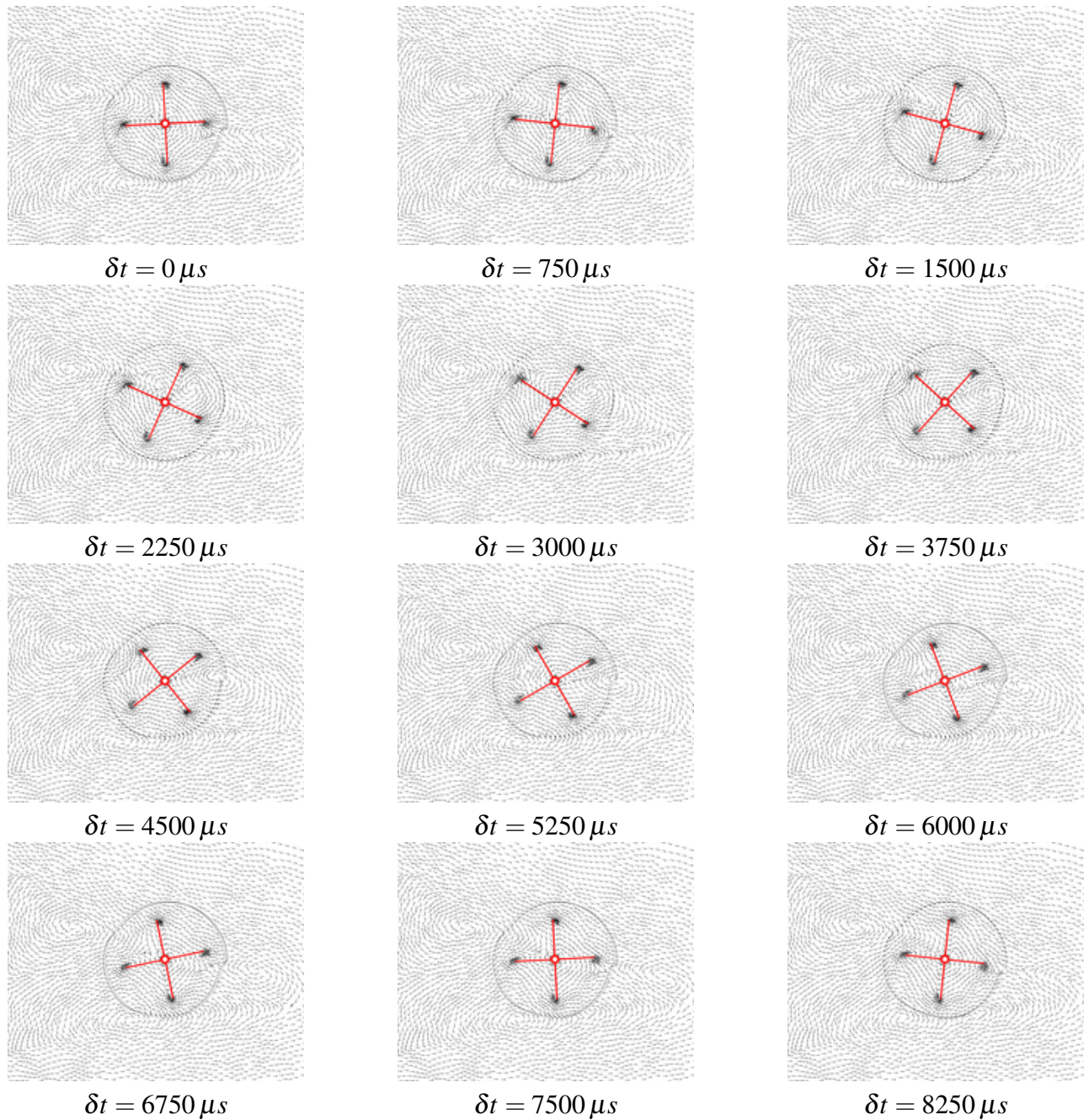


Figure 16: Direction vectors of the flow around the paddle wheel of case 3 for one geometrical cycle ($7500 \mu s$). The cyclic flow behavior is apparent when comparing the last two snapshots with the first ones. The Ahmed body lies to the left of these figures.

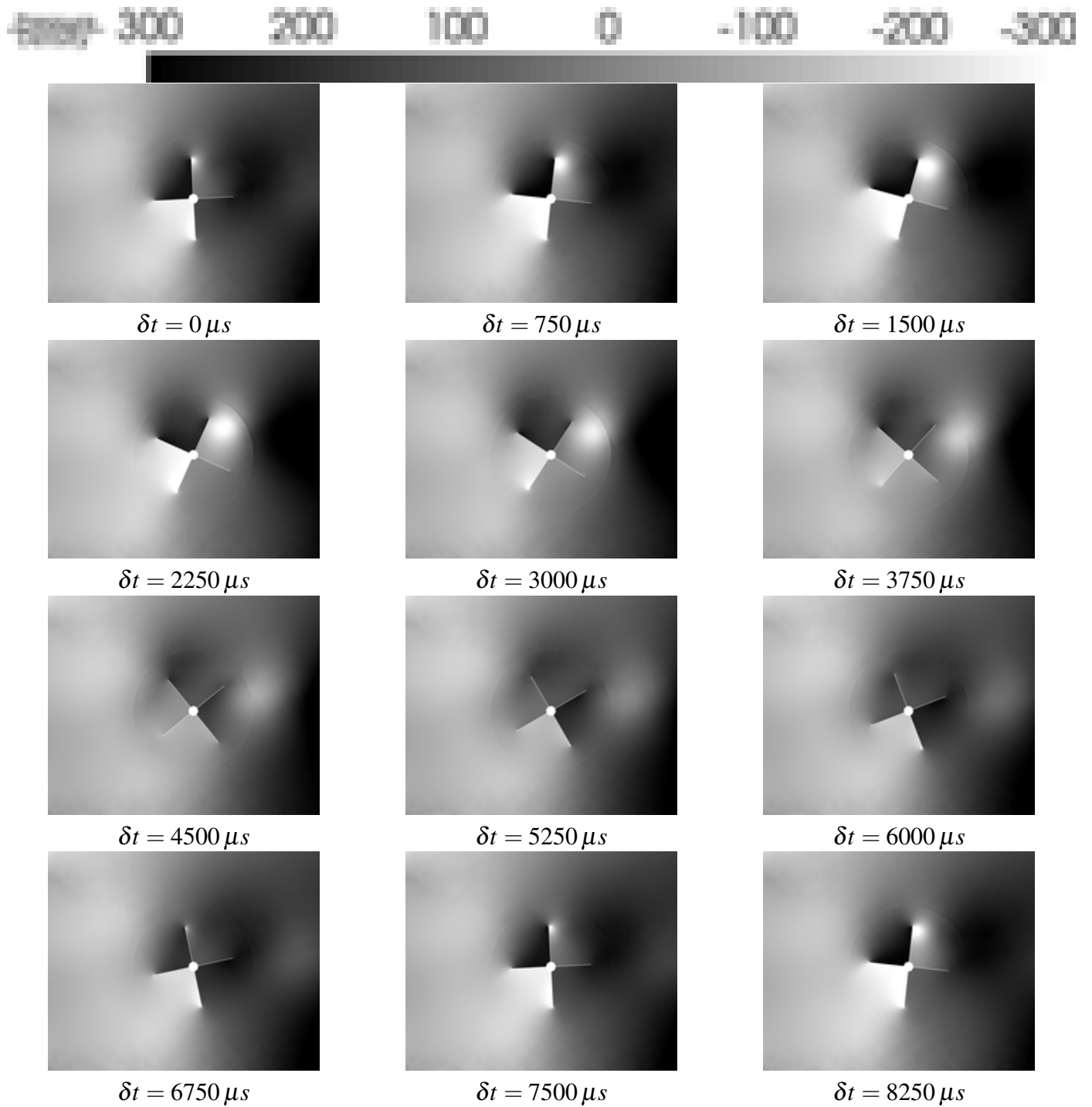


Figure 17: Pressure distribution of the flow around the paddle wheel of case 3 for one geometrical cycle ($7500 \mu s$). The cyclic flow behavior is apparent when comparing the last two snapshots with the first ones. The Ahmed body lies to the left of these figures.